Molecular dynamics analyses of CLDN15 pore size and charge selectivity

Sarah McGuinness, Pan Li, Ye Li**,** Shadi Fuladi, Sukanya Konar, Samaneh Sajjadi, Mohammed Sidahmed, Yueying Li, Le Shen*, Fatemeh Khalili Araghi*, Christopher R. Weber*

*Corresponding authors

SUMMARY Using cell culture and molecular dynamics simulations, we have clarified the role of amino acid D55 in the claudin-15 channel function. D55 is important for channel permeability and selectivity in both charge- and size-selective manners. This insight into the structural determinant of claudin cation channel function provides potential insight for designing approaches to alter the claudin channel function to benefit human health.

ABSTRACT The Claudin-15 (CLDN15) channel is important for nutrient, electrolyte, and water transport in the gastrointestinal tract. We used cell culture studies and molecular dynamics simulations to elucidate its structure and permeability mechanisms. We provide a model that underscores the crucial role of the D55 residue in the CLDN15 selectivity filter, which interacts with permeating cations. Our studies demonstrated the mechanisms whereby the size and charge of the D55 residue influence paracellular permeability. By altering D55 to larger, negatively charged glutamic acid (E) or similarly sized neutral asparagine (N), we observed changes in pore size and selectivity, respectively. D55E mutation decreased pore size, favoring small ion permeability without affecting charge selectivity, while D55N mutation led to reduced charge selectivity without markedly altering size selectivity. These findings shed light on the complex interplay of size and charge selectivity of CLDN15 channels. This knowledge can inform the development of strategies to modulate the function of CLDN15 and similar channels, which has implications for tight junction modulation in health and disease.

INTRODUCTION Claudins are a major component of tight junctions (Furuse et al., 2002; Gunzel and Yu, 2013; Tsukita et al., 2019). There are 27 members of the claudin family, and some of the claudins, such as claudin-2, -4, -10, and -15, are known to form paracellular ion channels (Rosenthal, 2017; Hou et al., 2010; Amasheh et al., 2002; Van Itallie et al., 2006; Günzel et al., 2009; Tamura, 2011). These channel forming claudins selectively regulate paracellular flux of molecules in a size and charge selective manner (Van Itallie et al., 2003; Salas and Moreno, 1982; Colegio, 2002). Claudins possess four transmembrane helices that are connected by intracellular and extracellular sequences (Suzuki, 2014). It is known that amino acid residues within the first extracellular region contribute to claudin charge selectivity (Gunzel and Yu, 2013; Krause, 2008; Colegio, 2003; Krause et al., 2009; Angelow and Yu, 2009). It has been hypothesized that structural differences between claudins can have profound effects on ionic interactions within the channel to affect small molecule permeability in a size and charge selective manner (Gunzel and Yu, 2013; Van Itallie et al., 2003; Alberini et al., 2018, 2017). Understanding how claudin tertiary structure regulates paracellular water and ion flux is central to defining how different claudins regulate extracellular fluid homeostasis in different kinds of epithelia, as well as the consequences of altered claudin expression or claudin mutations.

Although partial crystal structures of claudin-3, claudins-4, -15, and -19 have been resolved (Shinoda et al., 2016; Suzuki, 2014; Vecchio and Stroud, 2019; Nakamura et al., 2019; Saitoh et al., 2015), these structures cannot explain the interactions of claudins between cells, nor do they provide insight into the organization of claudin extracellular segments which define permeability. With this limited understanding of the biophysical basis of claudin-dependent tight junction permeability, it has been hypothesized that claudin channels are formed between two cells through the apposition of two antiparallel double rows of claudins (Suzuki, 2015). In an attempt to better understand the function of this model, we established an all-atom molecular dynamic simulation for claudin-15 (CLDN15; Samanta et al., 2018). The model defines the pathway for ion and water transport with a putative pore selectivity

filter at amino acid residue D55. However, in our previous study, we did not determine the mechanism whereby the selectivity filter could regulate both size and charge selectivity.

To address this question, we developed a reduced model which allowed us to extend our simulation durations at reduced computational cost, enabling us to perform simulations with multiple mutants and in a large number of conditions. Substitution of amino acid residue D55 with E or N dramatically alter the permeability characteristics of the CLDN15 pore. By altering D55 to larger, negatively charged glutamic acid (E) or similarly sized neutral asparagine (N), we observed changes in pore size and selectivity, respectively. D55E mutation decreased pore size, favoring small ion permeability without affecting charge selectivity, while D55N mutation led to reduced charge selectivity without markedly altering size selectivity. Our results demonstrate how a single amino acid residue change in the claudin pore selectivity filter can impart unique permeability characteristics.

MATERIALS AND METHODS

Generation of MDCK cells with inducible expression of CLDN15 and CLDN15 pore mutants.

Single vector-based Tet-inducible human claudin-15^{WT}, claudin-15^{D55E} and claudin-15^{D55N} expressing constructs were made similarly to previously described (Quintara Biosciences, Hayward, CA), (Samanta et al., 2018), and stably transfected into MDCK I cells along with a *PiggyBac* transposase encoding plasmid. After hygromycin selection, pooled clones were used for subsequent experiments.

Barrier function measurements in tissue cultured epithelial monolayers. MDCK I Cells were plated on 0.33 cm^2 polycarbonate semipermeable Transwell supports with 0.4 µm pores (Corning Life Sciences) at confluent density as previously described (Samanta et al., 2018). CLDN15 expression was induced using doxycycline (10–50 ng/ml) 1 d after plating. Doxycycline dosage was chosen to generate matched CLDN15 expression, as assessed by fluorescence microscopy. At day 5, cells were transferred to HBSS with 1 g/ml glucose and incubated at 37°C for 30 min prior to measurement of transepithelial electrical resistance (TER). Measured TER values were corrected for the resistance of the system in the absence of cells. Reversal potential measurements were performed using current clamp to I=0 in the setting of asymmetrical apical: basolateral ionic compositions. For NaCl dilution potentials, reversal potentials were measured with basal HBSS replaced by HBSS containing half the apical NaCl concentration (osmotically balanced with mannitol). From the reversal potential, the Goldmann–Hodgkin–Katz (GHK) equation was used to calculate the relative permeability of sodium to chloride ($V_{rev} = -(RT/F)\ln[(\alpha + \beta)/(1 + \alpha\beta)]$, where $\beta = PCl^-/PNa^+$, $\alpha = 1.9$, $RT/F = 26.6$). For biionic potentials, reversal potentials were measured with Na^+ of basal HBSS replaced by different monovalent cations. The GHK equation was used to calculate the permeability of different sized cations relative to Na^+ ($V_{rev} = (RT/F) \ln[(\gamma + \beta)/(1 + \beta)]$, where $\gamma = PM^+/PNa^+$)(Yu et al., 2009).

Molecular dynamics simulations. Molecular dynamics (MD) simulations were performed using the molecular dynamics program NAMD (Phillips et al., 2020). We used the CHARMM36 force field for proteins (Best, 2012; MacKerell, 1998; Mackerell Jr., 2004), ions (Beglov and Roux, 1994), phospholipids (Klauda et al., 2010), and TIP3 water model (Jorgensen, 1983). The updated nonbonded interactions between Na^+ and K^+ for their interaction with Cl^- were taken from (Luo and Roux, 2010) and applied through NBFIX. The forcefield parameters for methylammonium (MA^+), ethylammonium (EA^+), tetramethylammonium (TMA^+), and tetraethylammonium (TEA^+) were taken from the CHARMM General

ForceField (CGenFF). All simulations were carried out with periodic boundary conditions and a time step of 1 fs. Simulations were performed at constant temperature (333K) using Langevin dynamics with a friction coefficient of $\Upsilon = 5ps^{-1}$, and pressure was maintained at 1 atm using the Langevin Nose-Hoover method (Feller et al., 1995). We calculated the long-range electrostatic forces using the particle mesh Ewald algorithm with a grid spacing of 1 Å in each direction (Darden et al., 1993). A cutoff of 12 Å was used for non-bonded (short-range electrostatic and VdW) interactions (MacKerell, 1998).

System setup of CLDN15 (full channel). A full model of CLDN15 in two parallel POPC lipid bilayers was constructed based on our previously refined model of CLDN15 pores (Samanta et al., 2018). The unit cell in this model consists of 12 CLDN15 monomers forming three ion channels defining conductance in a plane parallel to the lipid bilayer. The entire system was comprised of 3.41×10^5 atoms.

To further improve the homogeneity of the system, the equilibrated conformation of the middle tetrameric pore was replicated to the other pores, and the system was further equilibrated at constant pressure. The lipid and water molecules were unaltered, and the system was ionized with NaCl at 213 mM. During equilibration, the protein backbone was initially constrained with a force constant of 1.0 kcal/mol·Å^2 and then gradually released to 0.75, to 0.50, to 0.25 and to 0.10 kcal/mol·Å^2 over a period of 30 ns. The constraints were then released for 10 ns, during which all three CLDN15 channels remained stable with an RMSD comparable to trajectories of our CLDN15 model published previously (Samanta et al., 2018).

Eight additional systems corresponding to LiCl, KCl, RbCl, CsCl, MACl, EACl, TMACl, and TEACl at 213 mM concentration were prepared by replacing Na^+ ions in the equilibrated full model (described above). Each new system was equilibrated for 5 ns at constant pressure to allow re-orientation of solvent around the ions. To prevent protein drift during simulations of ion transport, the backbone of the transmembrane (TM) helices anchoring the pores to the membrane were constrained with a force constant of 0.5 kcal/mol·Å^2 when applying a voltage bias.

Reduced model of CLDN15. We developed a reduced model of CLDN15 pores based on our previously published 3-pore model of CLDN15 (Samanta et al., 2018). In this model, part of the transmembrane (TM) helices of the proteins anchoring the pores to the membranes and their surrounding lipid membranes were omitted, leaving the ion conduction pore and its environment intact. The reduced model consists of the ion conduction pores and their surrounding solution with only 5.9×10^4 atoms.

To generate the reduced model, sections of the four TM helices enclosed by the lipid bilayer (CLDN15 residues 21 to 83 and 131 to 167) and the surrounding lipid membranes were removed. Water molecules between the two lipid bilayers were kept avoiding any changes in the ion conduction pores and their immediate surrounding. To emulate the anchoring role of the lipid bilayers, the four truncated TM helices were restrained in place by applying a harmonic constraint with a force constant of 5.0, 2.0, or 0.5 kcal/mol·Å^2 to the backbone of the last three helical turns of the reduced model (residues 21-26, 77-83, 131-136, and 161-167). Water molecules were constrained to the initial slab by applying a flat-bottom harmonic potential of 10.0 kcal/mol/Å^2 normal to the plane of membrane. The slab boundaries were chosen to match the equilibrated configuration, with a thickness of 30Å on the two sides of the pore and a thickness of 42Å in the middle of two rows. To avoid strong electrostatic interactions of the proteins with their periodic images, a periodic boundary was set in z-direction (normal to the membranes) 15 Å beyond the system.

This reduced model system was equilibrated for 105 ns with no additional restraints keeping the unit cell volume constant to assess its stability. This baseline system had an ion concentration of 306 mM.

Additional systems with reduced NaCl concentration of 153 mM and 100 mM was prepared by removing ions to reach the desired concentration and equilibrated for 20 ns. During the first 10ns the protein backbone was constrained. Additional systems containing LiCl, KCl, RbCl, CsCl, MACl, EACl, TMACl, and TEACl in place of NaCl were prepared and equilibrated for 5 ns to ensure proper hydration of ions and water reorientation prior to application of a voltage bias. Cations located inside the pore were moved to the bulk solution before replacing Na^+ with heavy cations to remove any bias for the low-conducting cations.

Mutant channels. Two CLDN15 mutants, $CLDN15^{D55E}$ and $CLDN15^{D55N}$, were constructed from the reduced model system. Starting from the $CLDN15^{WT}$ reduced model after 105 ns of equilibration, the two mutants were generated using VMD (Humphrey et al, 1996) to convert residue D55 on to glutamic acid (E) or asparagine (N). The systems were neutralized by adjusting the number of Cl^- ions and were equilibrated before applying a voltage bias. The protein backbone was constrained for the first 13 ns of equilibration, followed by 20 ns of unrestrained equilibration.

These NaCl mutant systems were then used to construct eight other systems by replacing NaCl with LiCl, KCl, RbCl, CsCl, MACl, EACl, TMACl, or TEACl. After ion replacement, each system was equilibrated for 10 ns with backbone constraints, followed by 30s of free run.

Ion transport simulations. The full model (WT) and the reduced model (WT and two mutants) systems were simulated under a voltage bias by application of a constant electric field along the channel's x-axis in order to study ion transport (Gumbart et al., 2012). Due to the continuous setup of claudin pores across the periodic boundaries, a constant electric field will result in uniform voltage bias across claudin pores without any additional leaks (voltage drops). This enables us to simulate the ionic currents under a constant voltage, and thus obtain the current-voltage (I-V) relationship of the channel and calculate the channel conductance.

The WT full model system was simulated with NaCl, LiCl, KCl, RbCl, and CsCl for 60 ns at ±100mV, ±200 mV, and ±400mV. The reduced model system at 153 mM salt concentration was simulated at ±200 mV, and ±400mV for 90 ns each and was used as the basis of comparison with the full model.

Reduced model systems (WT and two mutants) at 100 mM salt concentration were simulated at high voltages: ±800 mV and ±1200 mV for 30 ns each. The ionic current was calculated from the displacement charge of the ions over time at each voltage (Khalili-Araghi, 2013; Gumbart et al., 2012). The conductance was calculated as G=I/V.

Contact time and channel occupancy: The contact time of the ions with each amino acid residue within the channel was calculated from 10 ns of free run. Residues within 4 Å of the ions were selected, and the occupancy of each residue was calculated as the average number of ions in proximity of that residue. These trajectories were also analyzed to estimate the average occupancy of the ions per channel for each alkali cation system. Anions and cations residing with the channel were counted and averaged over simulation time.

Pore radius. The middle pore radius of each reduced model was calculated using the program HOLE (Smart et al, 1993) with MDAnalysis, resulting in time-averaged radius profiles for 10 ns equilibrated trajectories. 500 frames were used to calculate the pore radius.

Cation forcefield parameters (bulk conductivity). We used the same forcefield parameters in all of our simulations. These parameters were validated using simulations of bulk conductivity. For these simulations, we generated a 50 $Å^3$ pre-equilibrated water box containing 16 cations, 16 Cl^- ions and 3760 water molecules. The system was equilibrated for 1ns before applying a voltage bias of ±200 mV for 15 ns (constant volume, T=333 K) to generate a current. The last 11 ns of the simulation trajectory was used to determine the displacement charge and the solution conductivity similar to the other simulations reported here. We also measured bulk conductivity of the same ions by determining the I-V relationships of 100 mM X^+Cl^- solutions filled in polyethelene tubes. Conductance was normalized by tube length and cross-sectional area.

The simulated and measured conductivity values were similar, as determined by linear regression for solutions of LiCl, NaCl, KCl, RbCl, CsCl, MACl, TMACl (slope=1.21, R^2=0.99 at 100 mM and slope=1.06, R^2=0.94 at 1 M). This indicates that the forcefield parameters used in the simulations are reliable and provide a good approximation of the real-world behavior of the cations in this study.

RESULTS

We previously developed an all-atom model for CLDN15 quaternary structure, containing three ion pores (Priyanka et al., 2018; Fuladi et al., 2022b; a). Claudin monomers possess 4 transmembrane (TM) helices and two extracellular segments (ECS1 and ECS2). The claudin monomers assemble into an antiparallel double row of claudins in a single membrane, with extracellular β-sheets forming a half-pipe structure maintained by hydrogen bonds between β-strands (Suzuki, 2015, 2014). The pores are formed by two opposing half-pipes from two membranes and are sealed by hydrophobic trans-claudin interactions. The model, along with our cell culture studies, shows the importance of pore-lining residue D55 as a principal determinant of channel selectivity (Priyanka et al., 2018; Alberini et al., 2018, 2017).

CLDN15 D55 is a critical determinant of *in vitro* pore function. In order to define the potential electrostatic versus steric determinants of the key residue D55 on pore permeability properties, we developed MDCK monolayers which inducibly expressed wildtype CLDN15 (D55) or two different pore mutants. For the first mutant, aspartic acid was changed to similarly charged, but larger, glutamic acid (D55E). For the second mutant, aspartic acid was changed to similarly sized, but electroneutral asparagine (D55N). These mutations were chosen to evaluate the potential contributions of size and charge of amino acid residue responsible for the permeability filter (D55) to claudin-15 pore permeability.

Immunofluorescent staining revealed appropriate and similar expressions of $CLDN15^{WT}$, $CLDN15^{D55E}$, and $CLDN15^{D55N}$ at the tight junction (Fig. 1A). As expected for insertion of ion channels within the tight junction, expression of CLDN15and its mutants induced significant reductions in transepithelial electrical resistance (TER; Fig. 1B). We next determined relative permeabilities of Na^+ to Cl^- in these CLDN15 expressing monolayers by performing dilution potential measurements. The charge maintaining D55E mutation did not significantly alter PNa^+/PCl^- created by $CLDN15^{WT}$ expression, however the charge

neutralizing D55N mutation led to a significant reduction in CLDN15^{WT} expression caused charge selectivity (Fig. 1C).

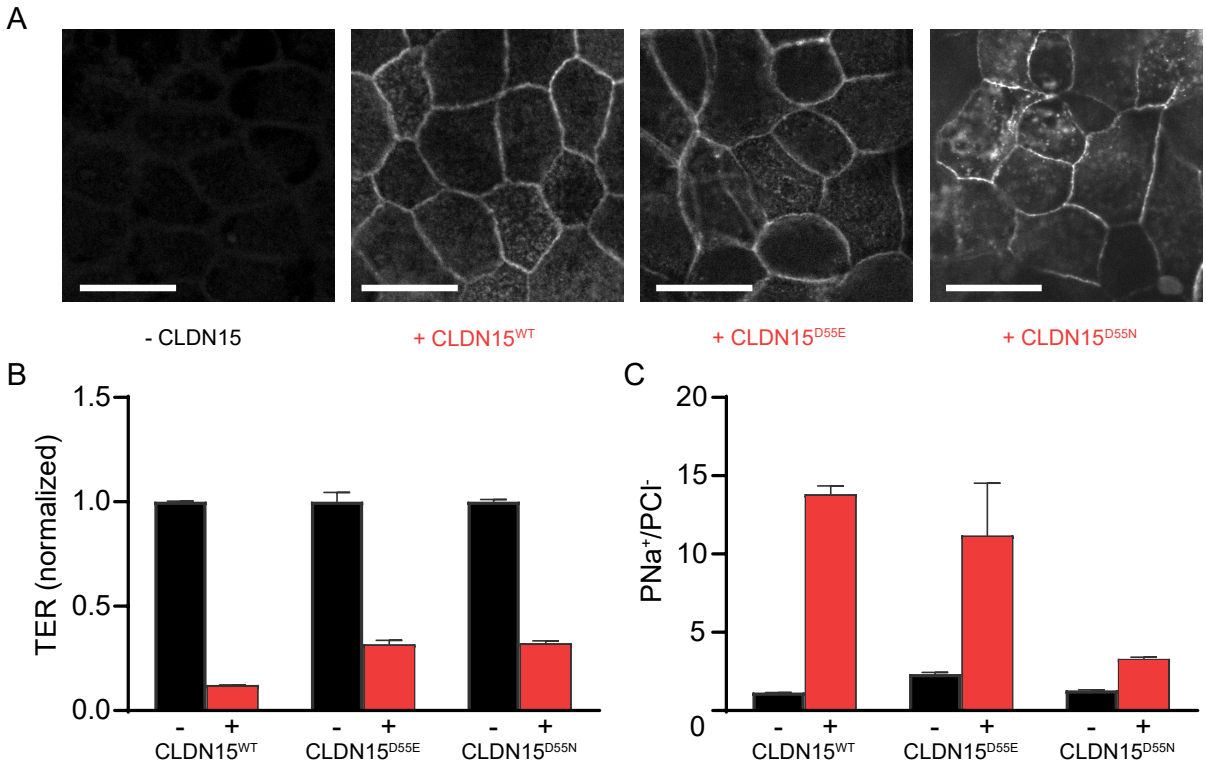

Figure 1: Generation and initial characterization of tet-inducible CLDN15-expressing MDCK I monolayers. (A) No CLDN15 expression was detected without doxycycline treatment. Following doxycycline treatment, wildtype CLDN15^{WT} or CLDN15^{D55E} and CLDN^{D55N} mutant was expressed at the tight junctions between cells (scale bar = 20 µm). **(B)** CLDN15 expression significantly reduced TER (avg±sem, n=4, all p<0.001) **(C)** and increased relative permeability of sodium to chloride (PNa$^+$/PCl$^-$) (avg±sem, n=4, all p<0.001).

To assess the contribution of CLDN15 D55 to channel size selectivity, we measured biionic potentials after basolateral substitutions of different sized cations for Na$^+$. This allowed calculation of the permeability of the substituted cation relative to Cl$^-$. The data are shown normalized to Cl$^-$ (Fig. 2A) or Na$^+$ (Fig. 2B). In all cell lines studied, without induced CLDN15 expression, permeabilities of different sized cations were low and size non-selective, consistent with the cell lines have no confounding selective conductance pathway for ions studied. For CLDN15^{WT} expressing monolayers, peak permeability was for cations with radii~ 1.5Å (K$^+$, Rb$^+$, and Cs$^+$) and was minimum for ions greater than radius 2.5Å (TMA$^+$ and TEA$^+$). CLDN15^{D55E} expressing monolayers exhibited a much different cation size selectivity profile with permeability decreasing as radii increased (from Na$^+$ to K$^+$, Rb$^+$, and Cs$^+$), with Cs$^+$ permeability being about half of peak ion permeability. CLDN15^{D55N} expressing monolayers also have an altered permeability profile. Similar to that of CLDN15^{WT} expressing monolayers, CLDN15 ^{D55N} have higher permeability for K$^+$ and Rb$^+$ relative to Na$^+$. In contrast, the permeability for larger ions, such as

Cs^+ and MA^+, was reduced in CLND15^{D55N} expressing monolayers relative to CLDN15^{WT} expressing monolayers, a phenomenon similarly found in CLDN15^{D55E} expressing monolayers. When comparing CLDN15^{D55E} and CLDN15^{D55N} expressing monolayers, Cs^+ permeability was reduced in both types of monolayers relative to peak permeability, but the permeability profile was right shifted by approximately 0.5 Å.

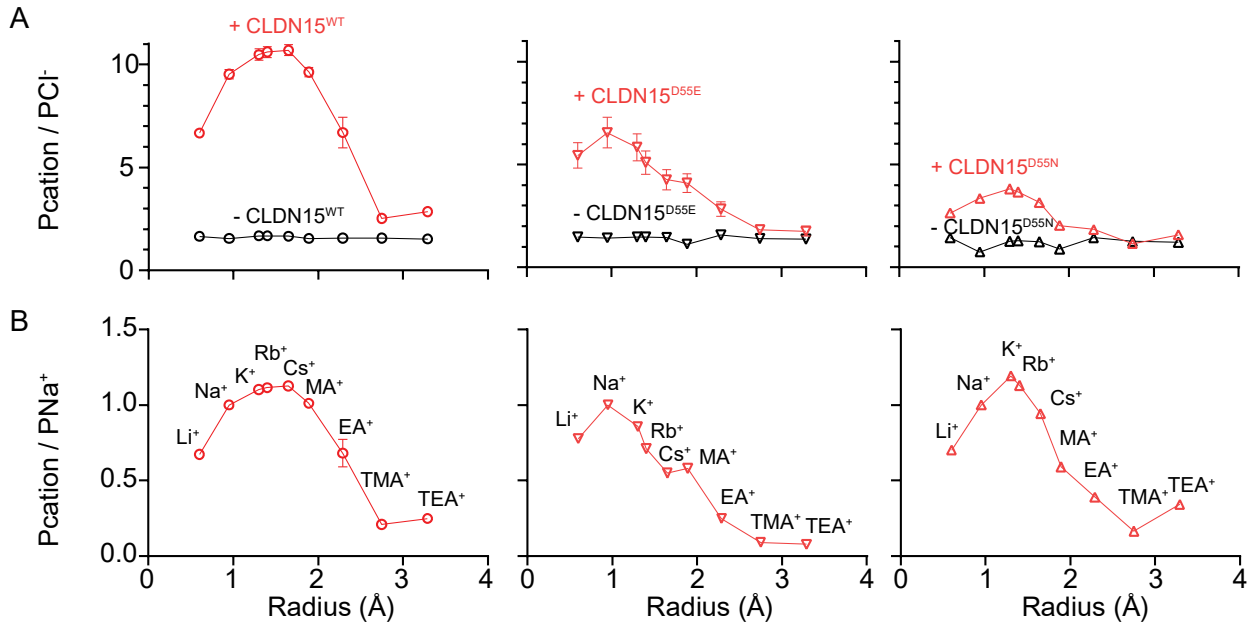

Figure 2: CLDN15^{D55E} and CLDN15^{D55N} mutants differentially affect pore charge and size selectivity profile. (A) Cation size selectivity was determined by using biionic potential measurements. CLDN15 expressing (red) and non-expressing (black) monolayers are shown. Cation permeabilities are normalized to chloride permeability to show charge selectivity as a function of cation size as well as the effects of D55E and D55N mutations. There was no charge selective barrier in control monolayers that did not express CLDN15, consistent with negligible baseline charge selectivity of the tight junction in parental MDCK I (mean ± SEM, n = 4) **(B)** The claudin-dependent size-selectivity profile for the same traces shown in A was calculated as the difference between cation permeability in monolayers that expressed or did not express claudin-15. Data are shown normalized to Na^+ and illustrate significant differences in the shape of the curves between WT and mutant CLDN15 constructs. (mean ± SEM, n = 4)

Molecular dynamic simulations of the CLDN15 pore. We hypothesized that these differences in permeability properties between CLDN15^{WT}, CLDN15^{D55E}, and CLDN15^{D55N} are due to unique interactions of permeating ions within the selectivity filter at residue 55. To test this, we turned to *in silico* modeling.

Beginning with our previously validated all atom CLDN15 model (Fig. 3A), we created a reduced model which enables longer simulations at reduced computational cost. This reduced model retains all of the amino acid residues within the pore region but omits the transmembrane regions that anchor the protein within the lipid bilayer. Despite these reductions, the ion conduction pore and its surrounding solution remain identical to the full all atom model. Through this reduced model, we achieved a six-fold improvement in computational efficiency compared to the full model. This substantial enhancement

permits the study of conductance across multiple mutants and the conductivity of a range of ions for each mutant. The sizes of the simulated cations are presented for comparison (Fig. 3B). In the model, when viewed along the pore axis, the presence of ions and water within the pore is evident (Fig. 3C). Viewing the model perpendicular to the pore, the apical and basolateral water compartments on either side of CLDN15 pore can be observed (Fig. 3D). The reduced model has considerably fewer elements, reduced from 3.41 x 10^5 atoms to 5.90 x 10^4 atoms. This simplification allows simulations to be extended six times longer for the same computational cost.

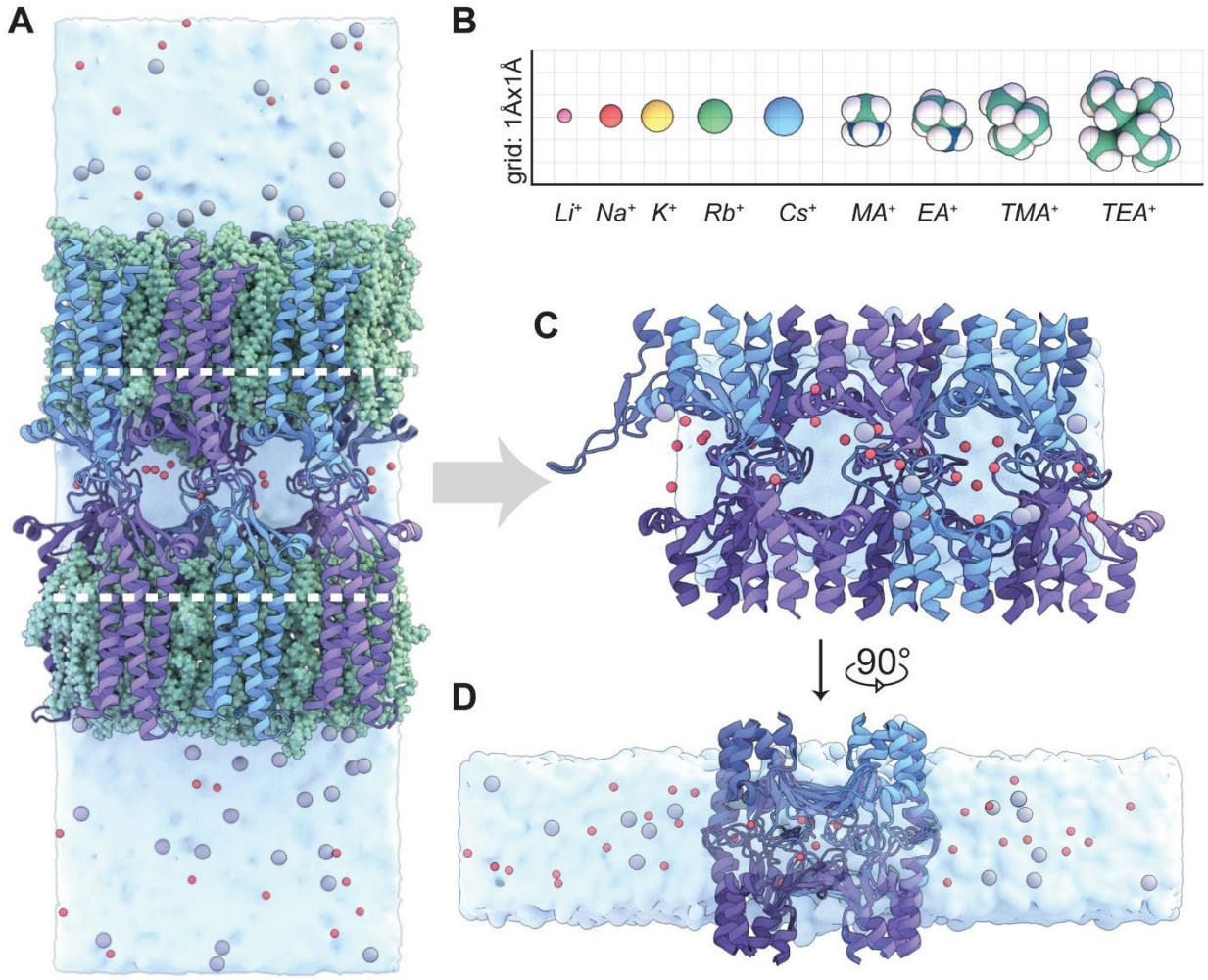

Figure 3: A reduced CLDN15 model allows for analysis of pore permeability properties. (A) A snapshot of the full CLDN15 model. The model contains two parallel lipid bilayers (green) and three CLDN15 pores, Na^+ (red), and Cl^- (gray), consisting of approximately 341,000 atoms. The white dotted lines indicate the section of protein removed in preparation for the reduced model. **(B)** Cations used in comparative simulations, plotted by size in Angstroms. **(C)** View of the channels in the reduced CLDN15 model. This model includes the ion conduction pores, surrounding solutions, and part of the transmembrane helices with only 59,000 atoms. **(D)** Side view of the reduced system model after a 90° counterclockwise rotation. The solutions on the two sides represent apical and basolateral solutions, however, it must be noted that the channel is symmetric.

We compared structural and functional properties of the reduced model (Fig. 3C, D) to the full model (Fig. 3A). The stabilities of the models were comparable. For the reduced model, the time-averaged backbone RMSD was 1.8±0.05 Å over 105 ns. The time-averaged RMSD 1.57±0.16 Å for the full model (P = 1 atm, temperature = 333 K); and the ion conduction pore was fully hydrated in both models. Like the full model, D55 remained the key amino acid residue interacting with cations (described below).

Cation conductance in the CLDN15 pore was determined through simulations of ion transport in the presence of a voltage gradient. In our previous study (Samanta et al., 2018), single-pore conductance values of Na^+ were 55.8 ± 16.8 pS. Similar values were obtained for the reduced model (56.7 ± 8.8 pS, 153 mM Na^+). To further investigate the relationship between cation size and conductivity, we examined the current-voltage relationship for cations of different sizes. This analysis allowed us to determine the conductivity profiles as a function of ion radius for both the full model (Fig. 4A, C) and the reduced model (Fig. 4B, D), which closely matched the experimentally derived cation permeability profiles (Fig. 2A, B left). The peak conductance values occurred at a cation radius of approximately 1.5 Å, between K^+ and Cs^+, which corresponds well with peaks in size-selective permeability determined in $CLDN15^{WT}$ expressing monolayers. Furthermore, similar to cell culture data, Cl^- conductance was much lower in both full model and reduced CLDN15 models (not shown).

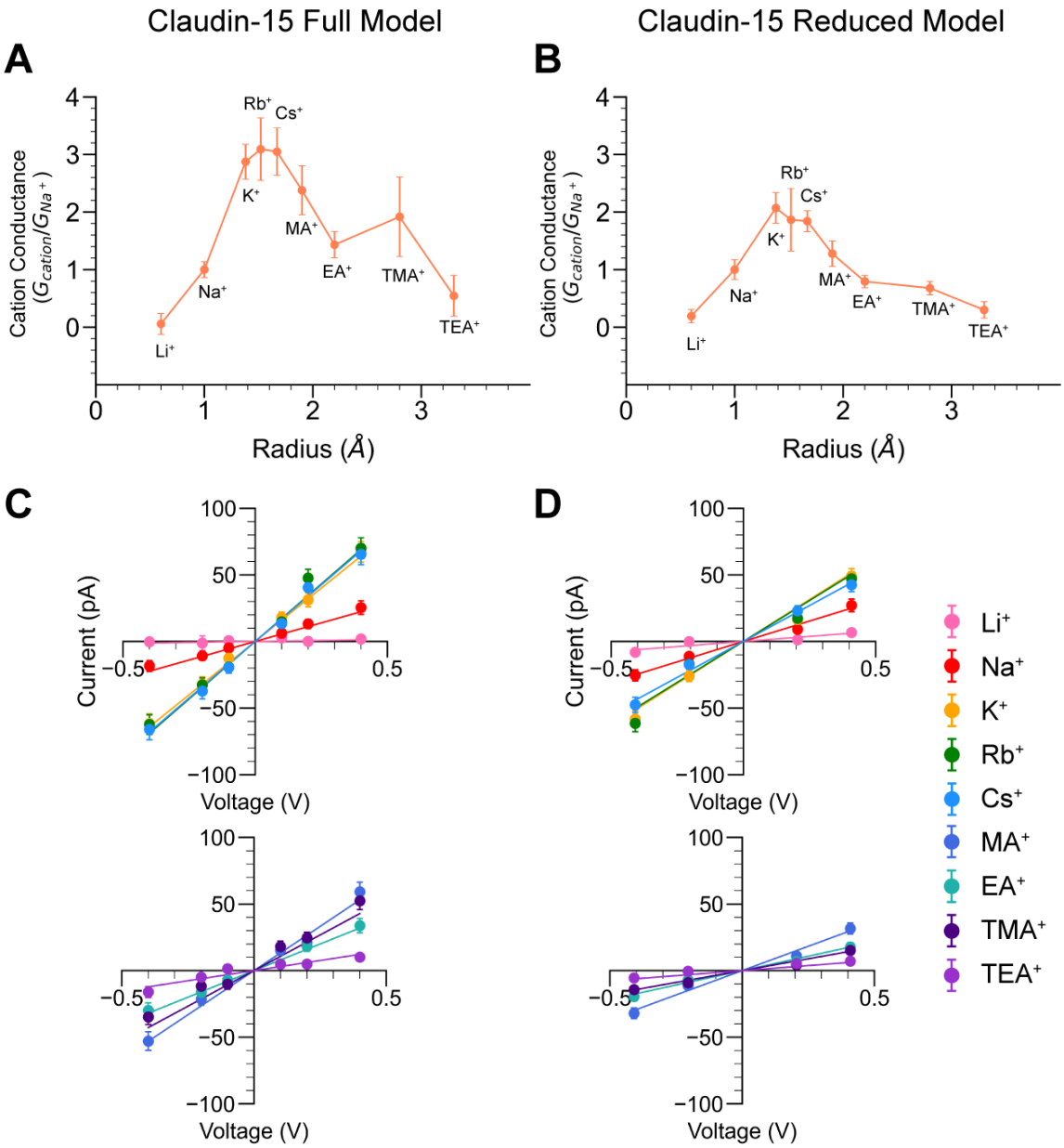

Figure 4: Ion channel property comparisons between full and reduced CLDN15 models. (A) Single-channel cation conductance of CLDN15^{WT} full model (213 mM cation concentration) normalized to sodium. **(B)** Single-channel cation conductance of CLDN15^{WT} reduced model (153 mM cation concentration) normalized to sodium. **(C)** I-V plots of the CLDN15^{WT} for ±0.1, ±0.2, and ±0.4V. **(D)** I-V plots of the reduced model CLDN15^{WT} at ±0.2V and ±0.4V.

Mutant size selectivity. Our cell culture data (Fig. 2) revealed differences in the size selectivity of conductance when D55 was mutated to E or N. We hypothesized that these differences were attributable to unique pore interactions between permeating cations and the selectivity filter as well as differences in the size of the pore. To evaluate the mechanism behind these differences, we simulated cation conductance profiles for the two mutants (Fig. 5A), in comparison with CLDN15^{WT}.

In the CLDN15^{WT} simulations, we observed peak cation conductance near the size of K^+ or Rb^+ (1.4-1.5Å in radius). The CLDN15^{WT} pore features a cage-like structure comprising four D55 residues, which binds to and regulates the passage of ions to define permeability (Fig. 5B). CLDN15 mutants studied also adopted similar general pore organization.

CLDN15^{D55E} mutation led to a leftward shift in peak conductance, with decreasing conductance for cations larger than K^+. This pattern was also observed from cell culture study results (Fig. 5 vs. Fig. 2), albeit slightly shifted to the right. The most significant effect of D55E mutation was a substantial reduction in Rb^+ and Cs^+ conductance compared to peak conductance, consistent with our cell culture data. CLDN15^{D55N} mutation resulted in a cation selectivity profile that closely resembled the CLDN15^{WT} simulations, with peak conductance shifted rightward toward larger cations. Peak conductance aligned more closely with the values observed for K^+ and Rb^+, which was comparable to the cell culture recordings.

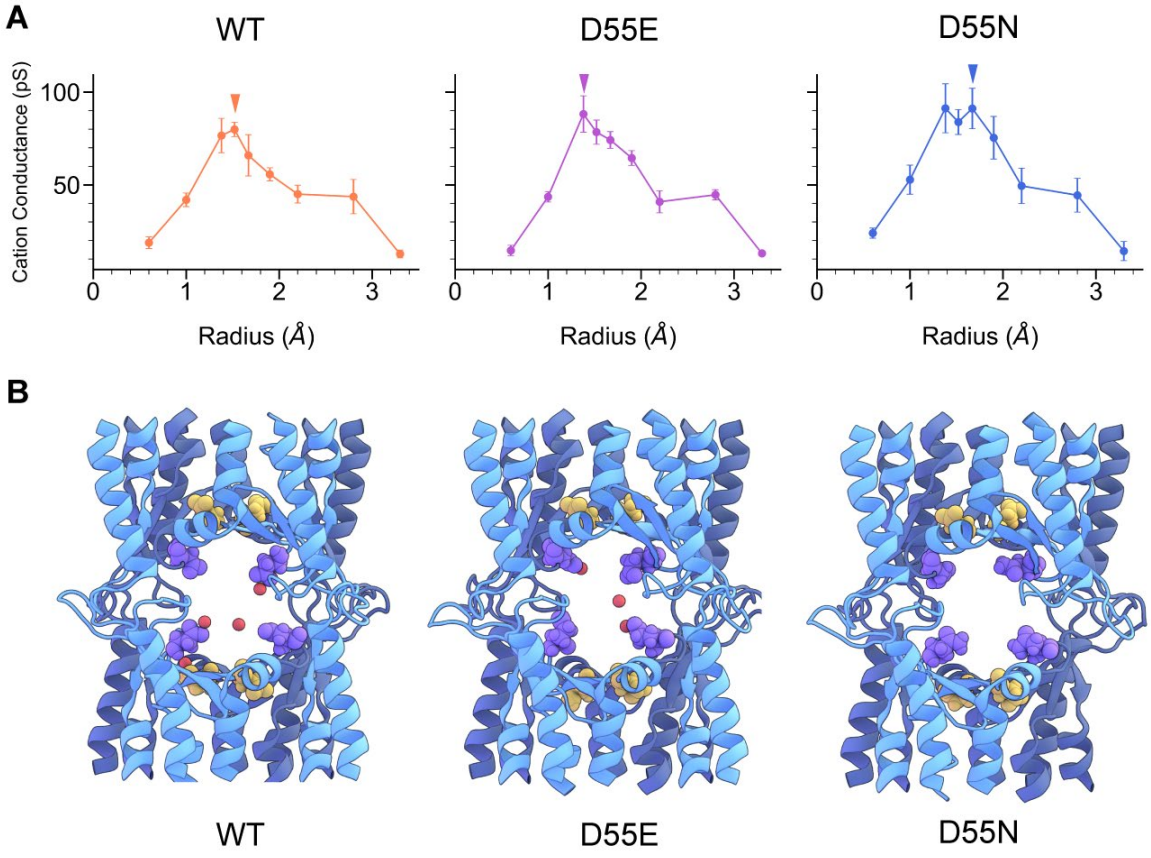

Figure 5: Mutant conductivity. (A) Single-channel cation conductance of CLDN15^{WT}, CLDN15^{D55E}, and CLDN15^{D55N} at 100mM cation concentration. Data points correspond to Li^+, Na^+, K^+, Rb^+, Cs^+, MA^+, EA^+, TMA^+, and TEA^+. **(B)** Snapshots of CLDN15 WT, D55E, and D55N channels taken from simulations. Residues 64 (yellow) and 55 (purple) can be seen interacting with Na^+ ions (red).

Pore Radius. We hypothesized that the difference between the CLDN15^{WT} and CLDN15^{D55E} permeability profiles could be due to a narrower pore radius for CLDN15^{D55E} in comparison to CLDN15^{WT} or CLDN15^{D55N} (Fig. 6). To assess this, we calculated the average pore radius profile for the channels along its conductivity pathway. Indeed, we observed that the CLDN15^{D55E} pore was narrower by 0.74 Å at the selectivity filter (Fig. 6). This could account for leftward shift in the peak of size-selective conductance observed in both simulated and cell culture studies.

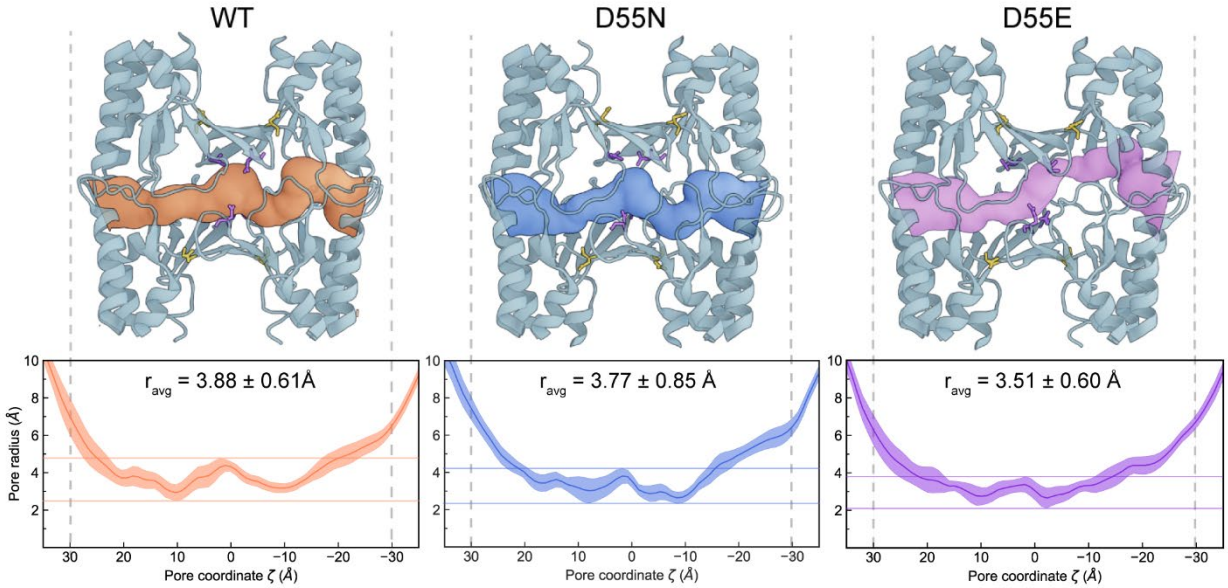

Figure 6: CLDN15 mutations affect pore radius profile. The mean pore radii (±SD) of CLDN15^{WT}, CLDN15^{D55E}, and CLDN15^{D55N} are 3.88±0.61 Å, 3.77±0.85 Å, and 3.51±0.60 Å, respectively. The minimum and maximum pore radius is marked with horizontal lines. The two pore-lining residues 55 and 64 in each pore are shown in purple and yellow, respectively.

Charge selectivity. We next assessed how D55 defines CLDN15 channel conductivities. Based on the contact time with the Na^+ ions (Fig. 7A), the negatively charged residue at position 55 (D55 in CLDN^{WT} or E55 in CLDN^{D55E}) had strong interactions with cations (Fig. 7A). On average, there were at least 2 cations bound to D55 (or E55) in the pore at all times, with an overall pore occupancy of ~5 cations (Fig. 7B). In contrast, overall pore occupancy for CLDN15^{D55E} was 2 cations per channel (Fig. 7B), likely due to the narrower pore radius at the permeability filter in CLDN15^{D55E} channels relative to CLDN15^{WT}. For both CLDN15^{WT} and CLDN15^{D55E} channels, secondary cation binding sites were observed near the extracellular helix (residues N61 and D64), which were bound approximately half the time. In contrast, Cl^- did not interact with these negatively charged amino acid residues (data not shown). D55N mutation resulted in dramatically reduced cation contact at position 55 as well as other interactions sites (Fig. 7A), with significant reduction in pore occupancy (Fig. 7B). The data supports that D55 is important for cation recruitment into the pore, contributing to charge selectivity observed in our cell culture studies (Fig. 1C).

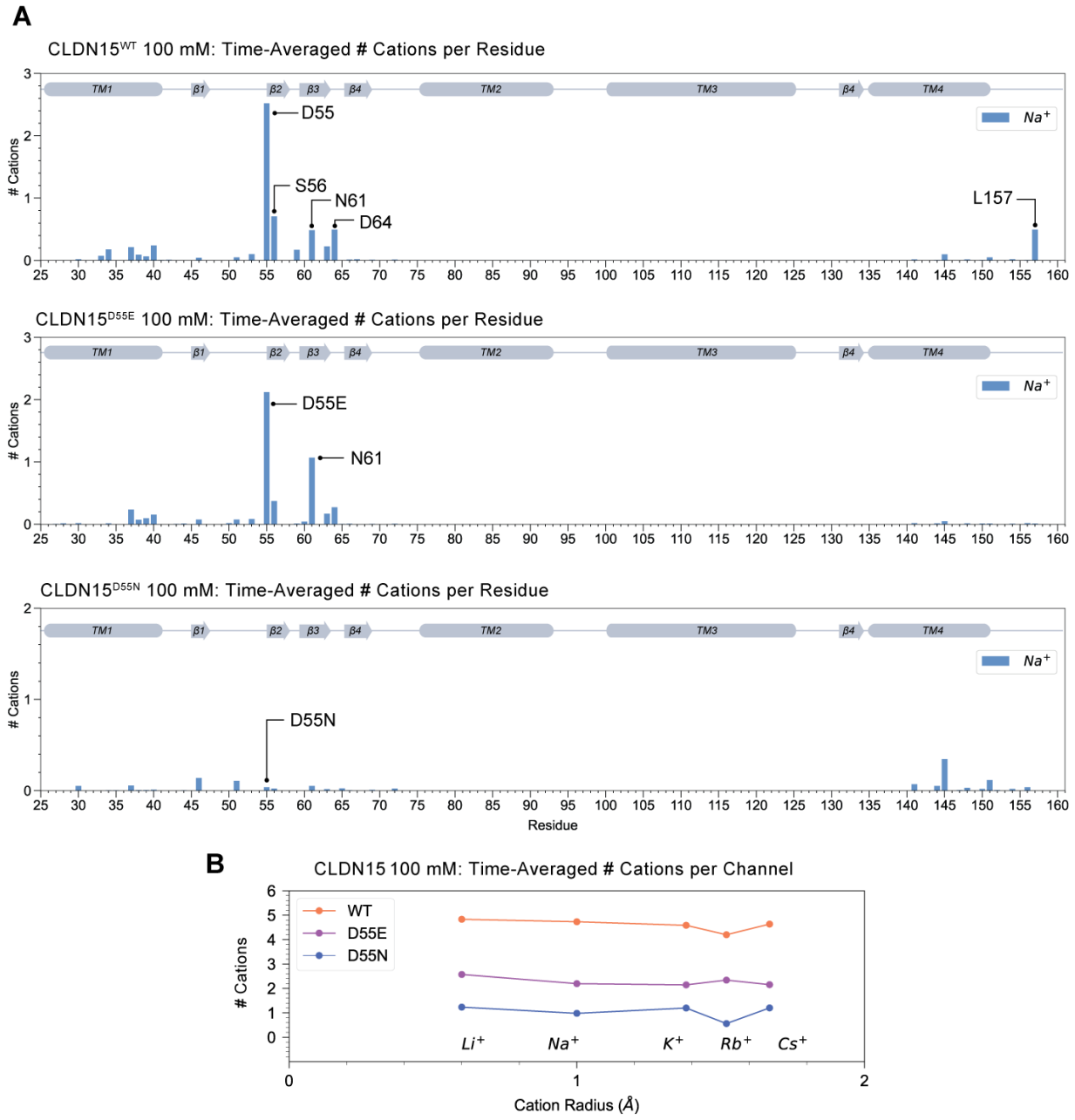

Figure 7: CLDN15 mutations affect channel occupancy and cation binding site (A) Histograms show the average number of Na^+ ions that can be found within contact of CLDN15 amino acid residues in simulation trajectories of CLDN15 WT, D55E, and D55N. **(B)** Average number of cations (Li^+, Na^+, K^+, Rb^+, Cs^+) within each pore for $CLDN15^{WT}$, $CLDN15^{D55E}$, $CLDN15^{D55N}$, calculated from equilibrium trajectories.

Discussion

CLDN15 is known to play critical roles in nutrient, electrolyte, and water transport (Tamura, 2011; Tamura et al., 2008; Tsukita et al., 2019). It is well recognized that CLND15 creates a size- and cation-

selective channel. Our previous study using all atom molecular dynamic simulations and cell culture studies demonstrated that the D55 amino acid residue is located within the CLDN15 selectivity filter and serves as a significant monovalent cation binding site. With the CLDN15 channel, the four D55 amino acid residue side chains extend toward the center of the channel forming a cage-like structure attracting cations. Despite these findings, it is not clear how the D55 site may contribute to the size and charge selectivity of the CLDN15 channel. By using a combination of cell culture and molecular dynamics simulation studies, our investigation revealed key insights into these mechanisms.

We first developed a reduced CLDN15 model that contains the ion conduction pore of the CLDN15 complex and surrounding water and ions, with the transmembrane domains removed. Despite these simplifications, such a reduced CLND15 model contains all atoms within the conductivity pathway that describes channel conductance and selectivity analogous to that of the full model. This model significantly reduced computational cost, allowing us to perform simulations with longer durations leading to more accurate measurements. This also allowed us to explore more simulation conditions, including salt concentration and voltage.

By mutating the negatively charged D55 to a larger, negatively charged glutamic acid (E) and the similarly sized neutral asparagine (N), we were able to probe D55 amino acid residue's contribution to channel size and charge selectivity. D55E mutation CLDN15 notably decreased the pore size at the selectivity filter. This resulted in an effective pore radius of 3.51 Å, compared to 3.88 Å in $CLDN15^{WT}$ and altered size selectivity profile of monovalent cations. D55 mutation to similarly sized, but neutral asparagine (N) modified CLDN15 channel charge selectivity, with reduced cation selectivity, demonstrated by decreased Na^+ to Cl^- permeability ratio. These studies demonstrated that although D55 controls CLDN15 charge and size selectivity, it does so through different properties of the D55 amino acid side chain. This points to the possibility for targeted modification of amino acid residues within the selectivity filter to engineer claudin channels with different size and charge selective profiles.

Quantifications of the contact time of cations with pore residues and pore occupancy demonstrate that despite similar contact time between Na^+ and D55 or D55E, Na^+ has significantly reduced channel occupancy. Similar results were obtained when using other alkali cations (data not shown). This difference may be explained by reduced pore volume at the selectivity filter in $CLDN15^{D55E}$ channels.

In our simulations, despite significantly reduced channel occupancy for cations in $CLDN15^{D55E}$ and a more drastic decrease in $CLDN15^{D55N}$, overall cation conductance of $CLDN15^{D55E}$ and $CLDN15^{D55N}$ channels is similar to that of $CLDN15^{WT}$. This points to the possibility that channel occupancy is not the only determinant for ion permeation through CLDN15 channels. Our model suggests the channel conductivity is a function of ionic interaction with pore-lining residues, as well as the overall volume of the pore. Specifically, $CLDN15^{D55E}$ has a smaller pore compared to $CLDN15^{WT}$, but the increased interactions allow for similar conductivity despite its reduced occupancy.

Uniquely, our study provides a biophysical basis for understanding the combination of size and charge selectivity to claudin channel function. The channel conductivity is a function of ionic interaction with pore-lining residues defined in Fig. 6A, as well as the overall volume of the pore. Specifically, D55E is a smaller pore compared to WT, but the increased interactions allow for similar conductivity despite its reduced occupancy. D55N pore is larger than D55E, but the reduced interaction of the cations with the pore leads to lower conductivity compared to WT or D55E.

Despite these novel findings, our study is not without limitations. Notably, despite an overall concurrence between the effects of mutations on CLDN15 function *in silico* and *in vitro*, there are some small differences between calculated and measured conductivities. Specifically, although the general shift of permeability profiles for different monovalent ions amongst the WT and mutants of CLND15 are similar between cell culture studies and simulations, there are small discrepancies in the absolute permeability values. These could be caused by inaccuracies of simulations. For example, non-polarizable forcefields used in our simulations, inherently carry some degree of error in representing ion, protein, and water interactions. The finite length of the simulation, especially for ions with low conductivities, plays an important role in simulation accuracy. The accuracy of the simulation data improves with increasing simulation time as the number of transport events (n), especially for the ions with low conductivity (error ~ $(1/\sqrt{n})$) (Aksimentiev and Schulten, 2005; Khalili-Araghi, 2013).

Our findings further validate that our CLDN15 model accurately delineates the pore-lining residues and their location within the pore. However, the structure of CLDN15 pore is yet to be determined experimentally. As such, our model stands to be refined as new experimental data emerges.

In addition to providing detailed understanding of characteristics of ion permeation across CLND15 channels, our reduced CLDN15 model can be used as a tool to screen small molecules *in silico* for their ability to bind to CLDN15 channels. Employing a similar strategy, other claudin channels could be modeled to understand their transport property. These advances will eventually guide us to rationally design claudin mutants for selective transport of ions and other small molecules.

In summary, our findings demonstrate that amino acid residue D55 plays a pivotal role in defining properties of CLDN15 conductance. Cell culture studies and simulations show the significance of D55 in controlling permeability properties. While D55 is a key amino acid residue for both CLDN15 channel size and charge selectivity, these parameters are independently controlled by the size and charge properties of the D55 side chain, respectively. The results and tools developed in this report will not only advance our basic understanding of biophysical properties of CLDN15, but also provide potential entry points to regulate claudin functions to benefit human health.

Acknowledgments

This work was supported by National Institute of Health R01DK131542 and National Science Foundation grant MCB-1846021.This research is part of the Frontera computing project at the Texas Advanced Computing Center. Frontera is made possible by the National Science Foundation award OAC- 1818253.

The authors declare no competing financial interests.

Author contributions: All authors contributed to writing the manuscript. Fatemeh Khalili-Araghi, Christopher Weber, Le Shen, and Sarah McGuinness, and Shadi Fuladi designed the experiments and simulations. Sarah McGuinness, Shadi Fuladi, Sukanya Konar, and Samaneh Sajjadi carried out and analyzed simulations. Pan Li, Ye Li, Mohammed Sidahmed, and Yueying Li carried out and analyzed the *in vitro* experiments.

References

Aksimentiev, A., and K. Schulten. 2005. Imaging α-hemolysin with molecular dynamics: ionic conductance, osmotic permeability, and the electrostatic potential map. *Biophys. J.* 88:3745–3761. doi:10.1529/biophysj.104.058727.

Alberini, G., F. Benfenati, and L. Maragliano. 2017. A refined model of claudin-15 tight junction paracellular architecture by molecular dynamics simulations. *PLOS ONE*. 12:e0184190. doi:10.1371/journal.pone.0184190.

Alberini, G., F. Benfenati, and L. Maragliano. 2018. Molecular dynamics simulations of ion selectivity in a claudin-15 paracellular channel. *J. Phys. Chem. B*. 122:10783–10792. doi:10.1021/acs.jpcb.8b06484.

Amasheh, S., N. Meiri, A.H. Gitter, T. Schöneberg, J. Mankertz, J.D. Schulzke, and M. Fromm. 2002. Claudin-2 expression induces cation-selective channels in tight junctions of epithelial cells. *J. Cell Sci.* 115:4969–4976. doi:10.1242/jcs.00165.

Angelow, S., and A.S. Yu. 2009. Structure-function studies of claudin extracellular domains by cysteine-scanning mutagenesis. *J Biol Chem*. 284:29205–17.

Colegio, O.R. 2002. Claudins create charge-selective channels in the paracellular pathway between epithelial cells. *Am J Physiol Cell Physiol*. 283:142–7.

Colegio, O.R. 2003. Claudin extracellular domains determine paracellular charge selectivity and resistance but not tight junction fibril architecture. *Am J Physiol Cell Physiol*. 284:1346–54.

Darden, T., D. York, and L. Pedersen. 1993. Particle mesh Ewald: An $N \cdot \log(N)$ method for Ewald sums in large systems. *J. Chem. Phys.* 98:10089–10092. doi:10.1063/1.464397.

Fuladi, S., S. McGuinness, and F. Khalili-Araghi. 2022a. Role of TM3 in claudin-15 strand flexibility: A molecular dynamics study. *Front. Mol. Biosci.* 9:964877. doi:10.3389/fmolb.2022.964877.

Fuladi, S., S. McGuinness, L. Shen, C.R. Weber, and F. Khalili-Araghi. 2022b. Molecular mechanism of claudin-15 strand flexibility: A computational study. *J. Gen. Physiol.* 154:e202213116. doi:10.1085/jgp.202213116.

Furuse, M., M. Hata, K. Furuse, Y. Yoshida, A. Haratake, Y. Sugitani, T. Noda, A. Kubo, and S. Tsukita. 2002. Claudin-based tight junctions are crucial for the mammalian epidermal barrier : a lesson from claudin-1–deficient mice. *J. Cell Biol.* 156:1099–1111. doi:10.1083/jcb.200110122.

Gumbart, J., F. Khalili-Araghi, M. Sotomayor, and B. Roux. 2012. Constant electric field simulations of the membrane potential illustrated with simple systems. *Biochim. Biophys. Acta*. 1818:294–302. doi:10.1016/j.bbamem.2011.09.030.

Günzel, D., M. Stuiver, P.J. Kausalya, L. Haisch, S.M. Krug, R. Rosenthal, I.C. Meij, W. Hunziker, M. Fromm, and D. Müller. 2009. Claudin-10 exists in six alternatively spliced isoforms that exhibit distinct localization and function. *J. Cell Sci.* 122:1507–1517. doi:10.1242/jcs.040113.

Gunzel, D., and A.S. Yu. 2013. Claudins and the modulation of tight junction permeability. *Physiol Rev*. 93:525–69.

Hou, J., A. Renigunta, J. Yang, and S. Waldegger. 2010. Claudin-4 forms paracellular chloride channel in the kidney and requires claudin-8 for tight junction localization. *Proc. Natl. Acad. Sci.* 107:18010–18015. doi:10.1073/pnas.1009399107.

Humphrey, W., A. Dalke, and K. Schulten. 1996. VMD: visual molecular dynamics. *J Mol Graph*.

Khalili-Araghi, F. 2013. Molecular dynamics simulations of membrane proteins under asymmetric ionic concentrations. *J Gen Physiol*. 142:465–475.

Krause, G. 2008. Structure and function of claudins. *Biochim Biophys Acta*. 1778:631–45.

Krause, G., L. Winkler, C. Piehl, I. Blasig, J. Piontek, and S.L. Müller. 2009. Structure and Function of Extracellular Claudin Domains. *Ann. N. Y. Acad. Sci.* 1165:34–43. doi:10.1111/j.1749-6632.2009.04057.x.

MacKerell, A.D.J. 1998. All-atom empirical potential for molecular modeling and dynamics studies of proteins. *J Phys Chem B*. 102:3586–3616.

Nakamura, S., K. Irie, H. Tanaka, K. Nishikawa, H. Suzuki, Y. Saitoh, A. Tamura, S. Tsukita, and Y. Fujiyoshi. 2019. Morphologic determinant of tight junctions revealed by claudin-3 structures. *Nat. Commun.* 10:816. doi:10.1038/s41467-019-08760-7.

Priyanka, S., W. Yitang, F. Shadi, Z. Jinjing, L. Ye, S. Le, W. Christopher, and K.-A. Fatemeh. 2018. Molecular determination of claudin-15 organization and channel selectivity. *J. Gen. Physiol.*

Rosenthal, R. 2017. Claudin-2-mediated cation and water transport share a common pore. *Acta Physiol.* 219:521–536.

Saitoh, Y., H. Suzuki, K. Tani, K. Nishikawa, K. Irie, Y. Ogura, A. Tamura, S. Tsukita, and Y. Fujiyoshi. 2015. Structural insight into tight junction disassembly by Clostridium perfringens enterotoxin. *Science*. 347:775–778. doi:10.1126/science.1261833.

Salas, P.J.I., and J.H. Moreno. 1982. Single-file diffusion multi-ion mechanism of permeation in paracellular epithelial channels. *J. Membr. Biol.* 64:103–112. doi:10.1007/BF01870772.

Shinoda, T., N. Shinya, K. Ito, N. Ohsawa, T. Terada, K. Hirata, Y. Kawano, M. Yamamoto, T. Kimura-Someya, S. Yokoyama, and M. Shirouzu. 2016. Structural basis for disruption of claudin assembly in tight junctions by an enterotoxin. *Sci. Rep.* 6:33632. doi:10.1038/srep33632.

Smart, O.S., J.M. Goodfellow, and B.A. Wallace. 1993. The pore dimensions of gramicidin A. *Biophys. J.* 65:2455–2460.

Suzuki, H. 2014. Crystal structure of a claudin provides insight into the architecture of tight junctions. *Science*. 18:304–307.

Suzuki, H. 2015. Model for the architecture of claudin-based paracellular ion channels through tight junctions. *J Mol Biol*. 427:291–297.

Tamura, A. 2011. Loss of claudin-15, but not claudin-2, causes Na+ deficiency and glucose malabsorption in mouse small intestine. *Gastroenterology*. 140:913–23.

Tamura, A., Y. Kitano, M. Hata, T. Katsuno, K. Moriwaki, H. Sasaki, H. Hayashi, Y. Suzuki, T. Noda, M. Furuse, S. Tsukita, and S. Tsukita. 2008. Megaintestine in Claudin-15–Deficient Mice. *Gastroenterology*. 134:523-534.e3. doi:10.1053/j.gastro.2007.11.040.

Tsukita, S., H. Tanaka, and A. Tamura. 2019. The Claudins: From Tight Junctions to Biological Systems. *Trends Biochem. Sci.* 44:141–152. doi:10.1016/j.tibs.2018.09.008.

Van Itallie, C.M., A.S. Fanning, and J.M. Anderson. 2003. Reversal of charge selectivity in cation or anion-selective epithelial lines by expression of different claudins. *Am. J. Physiol.-Ren. Physiol.* 285:F1078–F1084. doi:10.1152/ajprenal.00116.2003.

Van Itallie, C.M., S. Rogan, A. Yu, L.S. Vidal, J. Holmes, and J.M. Anderson. 2006. Two splice variants of claudin-10 in the kidney create paracellular pores with different ion selectivities. *Am. J. Physiol.-Ren. Physiol.* 291:F1288–F1299. doi:10.1152/ajprenal.00138.2006.

Vecchio, A.J., and R.M. Stroud. 2019. Claudin-9 structures reveal mechanism for toxin-induced gut barrier breakdown. *Proc. Natl. Acad. Sci.* 116:17817–17824. doi:10.1073/pnas.1908929116.